On the origin of shape fluctuations of the cell nucleus

Fang-Yi Chu[a], Shannon C. Haley[a], and Alexandra Zidovska[a,1]

[a]Center for Soft Matter Research, Department of Physics, New York University, New York, NY 10003

Edited by David A. Weitz, Harvard University, Cambridge, MA, and approved August 15, 2017 (received for review February 10, 2017)

The nuclear envelope (NE) presents a physical boundary between the cytoplasm and the nucleoplasm, sandwiched in between two highly active systems inside the cell: cytoskeleton and chromatin. NE defines the shape and size of the cell nucleus, which increases during the cell cycle, accommodating for chromosome decondensation followed by genome duplication. In this work, we study nuclear shape fluctuations at short time scales of seconds in human cells. Using spinning disk confocal microscopy, we observe fast fluctuations of the NE, visualized by fluorescently labeled lamin A, and of the chromatin globule surface (CGS) underneath the NE, visualized by fluorescently labeled histone H2B. Our findings reveal that fluctuation amplitudes of both CGS and NE monotonously decrease during the cell cycle, serving as a reliable cell cycle stage indicator. Remarkably, we find that, while CGS and NE typically fluctuate in phase, they do exhibit localized regions of out-of-phase motion, which lead to separation of NE and CGS. To explore the mechanism behind these shape fluctuations, we use biochemical perturbations. We find the shape fluctuations of CGS and NE to be both thermally and actively driven, the latter caused by forces from chromatin and cytoskeleton. Such undulations might affect gene regulation as well as contribute to the anomalously high rates of nuclear transport by, e.g., stirring of molecules next to NE, or increasing flux of molecules through the nuclear pores.

nuclear envelope | chromatin | nuclear lamina | active materials

The cell nucleus changes its shape and size dramatically during the cell cycle (1, 2). Such changes correspond to, e.g., decondensation of chromosomes in a newly formed nucleus, or, later, chromosome duplication, and occur on time scales of hours (3). Recently, small oscillations of nuclear area were found for stem cells and fibroblasts at time scales of minutes and attributed to local changes in chromatin compaction and cytoskeletal forces (4, 5). Shape fluctuations at even shorter time scales, "flickering," were previously studied only in membraneous systems, e.g., lipid vesicles, plasma membrane of red blood cells, and macrophages (6–8), where they were found to be largely thermally driven. Flickering of the cell nucleus, which has a more complex architecture, remains to be shown and characterized.

The shape of the cell nucleus is defined by the nuclear envelope (NE), a complex structure that confines chromatin, forming a physical boundary between the nucleoplasm and cytoplasm. NE comprises two lipid bilayers separated by a perinuclear space of 20 nm to 40 nm and supported from inside by nuclear lamina, a 50- to 80-nm-thick network formed by intermediate filament lamins (9, 10), which are presumed to provide NE with its structural support (11–13). Furthermore, NE is perforated by thousands of nuclear pores, gigantic protein complexes with diameter $\sim$120 nm and depth $\sim$45 nm, which aid the molecular transport into and out of the cell nucleus (14, 15). The presence of nuclear pores in the NE is integral to the NE's mechanical properties (16, 17).

Since NE is sandwiched between two active systems inside the cell—cytoskeleton on the cytoplasmic side and chromatin on the nucleoplasmic side—both could contribute to the nuclear shape fluctuations. Moreover, cytoskeleton as well as chromatin maintain direct links with NE (e.g., LINC complex, emerin, MAN1) (19, 20). Recent studies in yeast showed that microtubules were involved in the nuclear shape fluctuations over minutes, while chromatin tethering to NE influences nuclear deformability (21). In mammalian cells, cytoskeletal perturbations lead to changes in nuclear deformability (5), whereas chromatin interacts with NE via hundreds of lamina-associated domains, which reshuffle stochastically inside the nucleus (22). In fact, chromatin's interaction with NE is implicated in regulation of some genes (23–25).

Structural and functional errors of the NE lead to a large number of developmental and inherited disorders, so-called nuclear envelopathies, such as cardiomyopathy, muscular dystrophy, mandibuloacral dysplasia, and Hutchinson–Gilford progeria, as well as cancer (20, 26). Two major working hypotheses for these diseases are defects in gene regulation and abnormalities in nuclear architecture (27). Thus, elucidating mechanics of the nuclear shape fluctuations might contribute to the efforts to understand the NE in health and disease.

In this work, we study the flickering of the cell nucleus, i.e., nuclear shape fluctuations at short time scales of tens of seconds with temporal resolution of 250 ms. We monitor dynamics of both chromatin and nuclear envelope (NE) in live human cells. Using spinning disk confocal microscopy (*Materials and Methods*), we recorded high-resolution streams of live cells and studied the shape fluctuations for both the chromatin globule surface (CGS) visualized by GFP-tagged histone H2B (H2B-GFP) and the NE visualized by GFP-tagged lamin A (LMNA-GFP) (Fig. 1).

Results and Discussion

In Vivo Measurements of Nuclear Shape Fluctuations. To measure the shape fluctuations of CGS and NE as a function of time, we detected the contours of CGS (Fig. 1*B*) and NE (Fig. 1*E*) in every frame of the streams (*Materials and Methods*) and analyzed their dynamics. As shown in Fig. 1 *B* and *E*, *Insets*, the contours exhibit pronounced local shape fluctuations in time with amplitudes u of 100 nm to 200 nm in both directions (Fig. S1). We calculated u, which is the deviation of the instantaneous contour $r(\phi, t)$ from the average contour $r_0(\phi)$, by $u(\phi, t) = r(\phi, t) - r_0(\phi)$ at different times t. To focus on the amplitude of both inward and outward fluctuations, we computed u^2 for

Significance

While it is known that the shape and size of the cell nucleus change dramatically during the cell cycle, we find that the cell nucleus also exhibits subtle, but measurable, fast shape fluctuations at seconds. We find that the amplitude of these fluctuations systematically decreases during the cell cycle, thus serving as a reliable cell cycle stage indicator. Our findings show that the nucleus undergoes both thermally and actively driven undulations, the latter caused by forces from chromatin and cytoskeleton. Such undulations might affect gene regulation as well as aid the nuclear transport. Understanding the mechanism behind such undulations could prove critical for illuminating dynamic behavior of the nucleus in health and disease.

Author contributions: A.Z. designed research; F.-Y.C. and A.Z. performed research; F.-Y.C., S.C.H., and A.Z. contributed new reagents/analytic tools; F.-Y.C. and A.Z. analyzed data; and F.-Y.C. and A.Z. wrote the paper.

The authors declare no conflict of interest.

This article is a PNAS Direct Submission.

[1]To whom correspondence should be addressed. Email: alexandra.zidovska@nyu.edu.

This article contains supporting information online at www.pnas.org/lookup/suppl/doi:10.1073/pnas.1702226114/-/DCSupplemental.

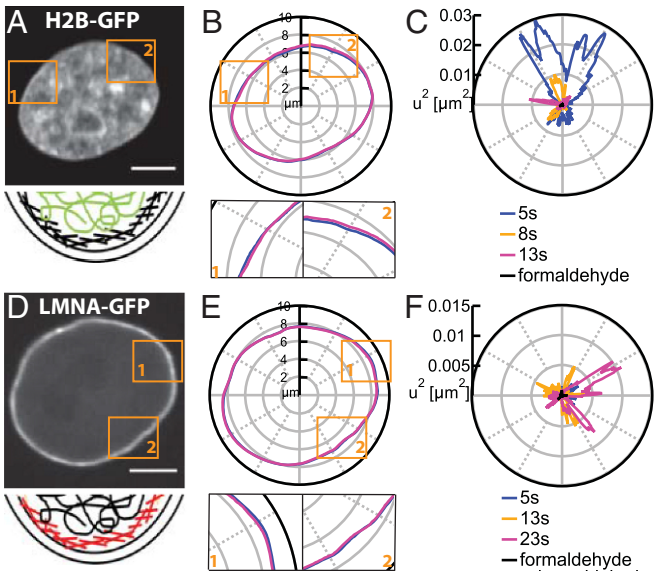

Fig. 1. In vivo measurements of shape fluctuations of CGS and NE. (*A*) A micrograph of cell nucleus expressing H2B-GFP and schematics of the localization of chromatin (green) relative to the NE (black). (*B*) Contours of CGS at t = 5 and 13 s. *Insets* 1 and 2 present a zoomed in view. (*C*) Fluctuations u^2 of CGS at t = 5, 8, and 13 s and for nucleus fixed with formaldehyde (black dot at the origin) demonstrating that our measurements are well above the noise floor. (*D*) A micrograph of cell nucleus expressing LMNA-GFP and schematics of the localization of lamins (red) relative to chromatin (black) and two lipid bilayers (black) comprising the NE. (*E*) Contours of the NE at t = 5 and 23 s. *Insets* 1 and 2 present a zoomed in view. (*F*) The u^2 of NE at t = 5, 13, and 23 s. (Scale bar, 5 μm.)

CGS and NE, respectively. Fig. 1 *C* and *F* shows u^2 for CGS and NE at three different time points, demonstrating their dynamic behavior. As a negative control, we measured u^2 for cells fixed in formaldehyde and found the shape fluctuations to be eliminated (Fig. 1 *C* and *F*), showing that our measurements are well above the noise floor.

Further, to determine the wavenumber-dependent shape fluctuations of the CGS and NE, we performed the Fourier transformation of $u(\phi, t)$ at every time t following $u_q(t) = 1/2\pi \int_0^{2\pi} u(\phi, t) e^{-iq\phi}\, d\phi$ and calculated the mean-square amplitude $\langle u_q^2 \rangle$ as described in ref. 7 (*SI Materials and Methods*). We computed $\langle u_q^2 \rangle$ as a function of modal wavenumber q for both CGS and NE. Fig. 2*A* shows $\langle u_q^2 \rangle$ averaged over 47 nuclei for both CGS and NE, which are similar in their amplitude and q dependence (Fig. S2). As a negative control, we carried out the same calculation for cells fixed in formaldehyde (Fig. 2*A*), which shows elimination of shape fluctuations upon fixation.

To gain insight into the population average $\langle u_q^2 \rangle$ from Fig. 2*A*, we reviewed the $\langle u_q^2 \rangle$ distribution at every q separately. Fig. 2*B* shows examples of histograms for $\langle u_q^2 \rangle$ at $q = 2$ and $q = 6$ for both CGS and NE. We found the $\langle u_q^2 \rangle$ distributions to have quite complex shapes for both CGS and NE, suggesting a presence of more than one contributing population. For example, $\langle u_q^2 \rangle$ at $q = 2$ for NE shows two modes, one at low and one at high $\langle u_q^2 \rangle$. A careful inspection of the $\langle u_q^2 \rangle$ distributions revealed that different modes correspond to different sizes of the cell nuclei. To further explore this finding, we sorted the nuclei by their area into four groups (with n being the number of nuclei in the group) for CGS—A_1 = 140 μm² to 170 μm² (n = 11), A_2 = 170 μm² to 190 μm² (n = 11), A_3 = 190 μm² to 210 μm² (n = 16), and A_4 = 210 μm² to 240 μm² (n = 9)—and for NE—A_1 = 160 μm² to 210 μm² (n = 10), A_2 = 210 μm² to 240 μm² (n = 10), A_3 = 240 μm² to 260 μm² (n = 11), and A_4 = 260 μm² to 345 μm² (n = 16). Fig. 2*C* shows the average $\langle u_q^2 \rangle$ for all four groups for CGS (green) and NE (red). Remarkably, there was a clear decrease of $\langle u_q^2 \rangle$ with increasing nuclear size, while we found no correlation with the nuclear shape (Fig. S3). Thus, we hypothesized that, since the nuclear size is known to be cell cycle-dependent (1, 2), the $\langle u_q^2 \rangle$ is cell cycle-dependent.

Nuclear Shape Fluctuations During Cell Cycle. To test our hypothesis, we obtained $\langle u_q^2 \rangle$ as a function of cell cycle progression. We synchronized both HeLa H2B-GFP and HeLa LMNA-GFP cells (*Materials and Methods*) and measured $\langle u_q^2 \rangle$ as well as nuclear size for 31 h, where $t = 0$ h corresponds to metaphase. We collected data at six time points: $t = 1, 7, 13, 19, 25$, and 31 h. Fig. 2*D* presents histograms of nuclear area for CGS and NE for different time points in the cell cycle, which clearly show the increase in the nuclear size with cell cycle progression. Fig. 2*E* presents four micrographs of the same HeLa H2B-GFP nucleus at four different time points, showing the monotonic increase in the size of the cell nucleus (corresponding data for HeLa LMNA-GFP are shown in Fig. S4). In addition, after we computed $\langle u_q^2 \rangle$ for the six time points, we found that $\langle u_q^2 \rangle$ clearly decreases with progressing cell cycle (Fig. 2 *F* and *G*), which is consistent with our original hypothesis. To quantify this phenomenon, we normalized $\langle u_q^2 \rangle$ at every time point by $\langle u_q^2 \rangle$ at t_1, for $q = 2$ and 5, for both CGS and NE. Fig. 2*H* shows a more than fivefold reduction of relative $\langle u_q^2 \rangle$ during the cell cycle for both CGS and NE, while the relative nuclear area A, i.e., A at different times normalized by A at t_1, shows almost a twofold increase, with the biggest changes found in G1 phase. Thus, strikingly, measuring $\langle u_q^2 \rangle$ allows us to determine the cell cycle stage in live cells. Using $\langle u_q^2 \rangle$ as a cell cycle stage reporter is noninvasive and requires only one fluorescent tag (labeling either NE or CGS).

The pronounced decrease of $\langle u_q^2 \rangle$ with the progress of cell cycle may be due to two main reasons: change of NE material properties (e.g., increase in its stiffness) or reduction of the forces driving the shape fluctuations. The former is consistent with our and others' observations of gradual deposition of lamin A into NE over hours after mitosis, which would make NE stiffer (Fig. S4 and ref. 28). This is supported by an observed cell cycle-dependent decrease of $\langle u_q^2 \rangle$ at high q, the part of the spectra that follows q^{-4} (Fig. S4), which would be expected from Helfrich theory for bending rigidity dominated thermal fluctuations (29). Furthermore, the forces driving the nuclear shape fluctuations might very well change with the cell cycle.

Coupling of CGS and NE Shape Fluctuations. Similar dynamic behavior of CGS and NE as evidenced by $\langle u_q^2 \rangle$ suggests that CGS and NE are dynamically closely related, possibly coupled. To investigate how the dynamics of CGS and NE are related, we visualize the shape fluctuations of CGS and NE simultaneously by transfecting HeLa LMNA-GFP cells with H2B-mCherry (Fig. 3*A* and *Materials and Methods*). We evaluated the extent of fluctuations by calculating the ratio $r_f = n_f / n_{tot}$ determined by counting the fluctuation sites n_f, where $u_{ne} \neq 0$ or $u_{cgs} \neq 0$, along the contour and normalized by the length of the contour (i.e., total number of sites n_{tot}); u_{cgs} and u_{ne} are the shape fluctuations of CGS and NE, respectively. We find that, at a given time, two thirds of the contour exhibits shape fluctuations. We measured the duration of the fluctuation events τ_f and found two types of events: $\tau_{f,1} < 1$ s and $\tau_{f,2} \approx 4$ s to 5 s. Further, we computed the rate of the fluctuation activity $k_f = \sum(\tau_{f,i}/t_{tot})$ for a fluctuation site to be, on average, 0.22, which we calculated as the time a fluctuation site is fluctuating per unit time, where t_{tot} is the length of the measurement (Fig. S5).

We found that, while CGS and NE typically fluctuate in phase, they do exhibit sites where they move out of phase, which we termed "separation sites." Fig. 3 *B* and *C* shows an example of

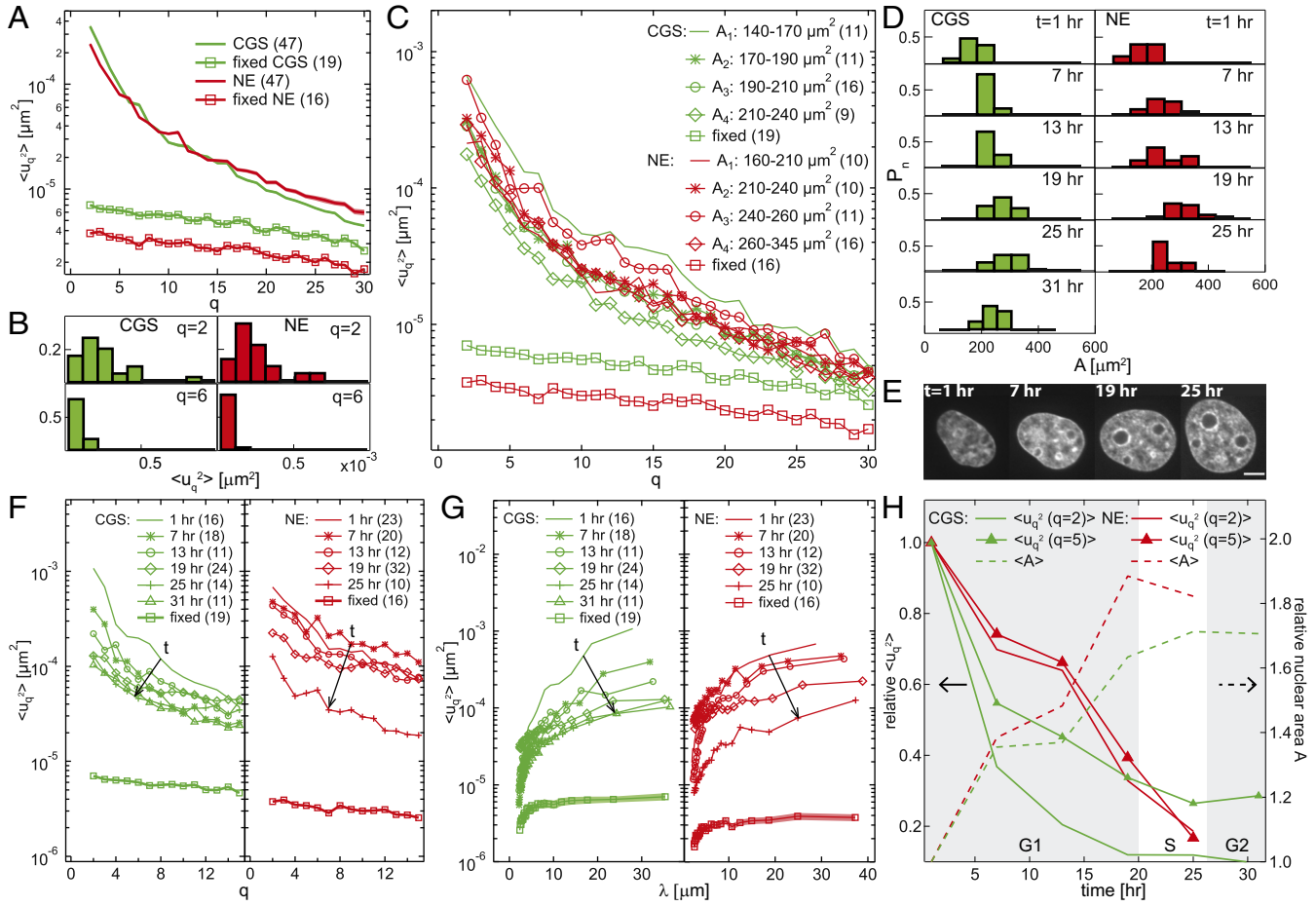

Fig. 2. Shape fluctuations of CGS and NE are cell cycle-dependent. (*A*) Wavenumber-dependent fluctuations $\langle u_q^2 \rangle$ for CGS (H2B-GFP, green line, $n = 47$) and NE (LMNA-GFP, red line, $n = 47$). As a negative control, we calculated $\langle u_q^2 \rangle$ for both CGS (green square markers, $n = 19$) and NE (red square markers, $n = 16$) after fixing with formaldehyde. (*B*) Histograms of $\langle u_q^2 \rangle$ for CGS and NE, at $q = 2$ and 6, respectively. (*C*) The $\langle u_q^2 \rangle$ of CGS and NE calculated separately for four groups based on their nuclear area A for CGS (green) and NE (red); $\langle u_q^2 \rangle$ for CGS decreases with the increasing A. (*D*) Histograms of nuclear area A measured for a synchronized cell population at $t = 1$, 7, 13, 19, 25, and 31 h after metaphase. The nuclear size increases for both CGS and NE with the progressing cell cycle. (*E*) Micrographs of the same nucleus at four different times, showing its size increase during the cell cycle. (Scale bar, 5 μm.) (*F*) The $\langle u_q^2 \rangle$ of CGS (green) and NE (red) measured at different times during the cell cycle; $\langle u_q^2 \rangle$ for both CGS and NE exhibits a monotonous decrease with increasing time (highlighted by the black arrow) with p value less than 0.05 for $t = 1$, 13, 25, and 31 h. (*G*) $\langle u_q^2 \rangle$ of CGS (green) and NE (red) from *F* plotted as a function of wavelength $\lambda = L_c/q$, where L_c is the contour length. (*H*) Relative $\langle u_q^2 \rangle$, i.e., $\langle u_q^2 \rangle$ at different times normalized by $\langle u_q^2 \rangle$ at $t = 1$ h, for $q = 2$ and 5, for CGS (green) and NE (red) decreases during G1, S, and G2 (timing from ref. 18), while the relative nuclear area A, i.e., the nuclear area at different times normalized by the nuclear area at $t = 1$ h, increases. Error bars for *A*, *C*, and *F*–*G* are shown in Fig. S2.

a separation site, which occurred at $t = 10$ s, but is no longer present at $t = 22$ s. The separation sites can be detected by comparing the simultaneous contours of CGS and NE (Fig. 3*D*, highlighted by blue arrow) as well as in the shape fluctuation amplitudes u^2 (Fig. 3*E*).

To analyze the extent and the temporal evolution of a separation site, we evaluated relative shape fluctuations of CGS and NE with respect to each other, which we defined as $(u_{ne} - u_{cgs})^2$. Fig. 3*F* shows a plot of $(u_{ne} - u_{cgs})^2$ as a function of time t and polar angle ϕ, which visualizes the temporal evolution of separation sites along the nuclear contour $r(\phi, t)$. The plot shows only the $(u_{ne} - u_{cgs})^2$ above the noise floor, which was determined by measurements in fixed cells. The separation sites undergo spurts of separation, which we named "separation events" and characterized by their duration time τ. The separation site in Fig. 3*F* shows several separation events of variable duration $\tau = 2$ s to 5 s.

We evaluated two types of separation ratios, $r_{s,tot} = n_s/n_{tot}$ and $r_{s,f} = n_s/n_f$, determined by counting the number of separation sites n_s along the contour and normalized by n_{tot} and n_f, respectively. We find that, at any given time, approximately 20% of the CGS and NE can fluctuate out of phase, as evidenced by $r_{s,tot}$, which corresponds to ~30% of the fluctuation sites, as evidenced by $r_{s,f}$. The rate of separation activity $k_s = \sum(\tau_{s,i}/t_{tot})$ was found to be about 0.07, which we calculated as the time a separation site is actually separated ($u_{ne} - u_{cgs} \neq 0$ above the noise floor) per unit time.

Origin of Nuclear Shape Fluctuations. To elucidate the origin of the shape fluctuations of CGS and NE, we used biochemical perturbations (Fig. 4). Specifically, to determine whether the observed dynamics of CGS and NE are actively driven, we depleted ATP (*Materials and Methods*). We found that both u^2 (Fig. 4*B*) and $\langle u_q^2 \rangle$ (Fig. 4*C*) were strongly reduced ($n = 24$), confirming that active processes indeed contribute to nuclear shape fluctuations. Furthermore, we explored the involvement of the cytoskeleton in the CGS and NE dynamics by measuring the shape fluctuations of CGS and NE upon inhibition of microtubule polymerization by nocodazole ($n = 18$), actin

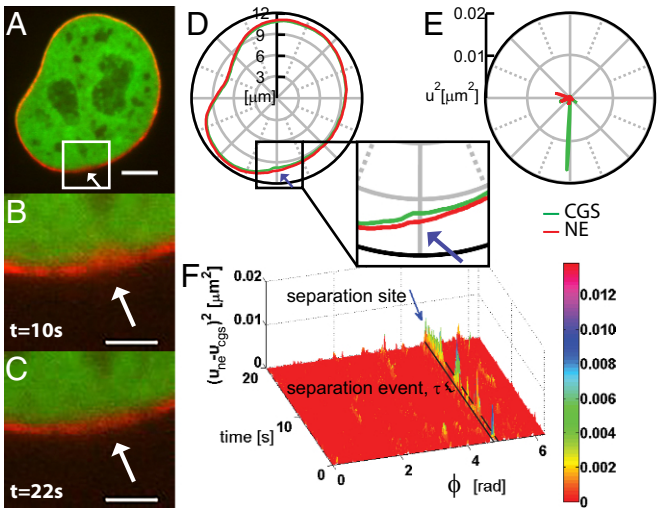

Fig. 3. Simultaneous measurements of shape fluctuations of CGS and NE. (*A*) A micrograph of a nucleus expressing both H2B-mCherry (green) and LMNA-GFP (red) obtained using simultaneous two-color confocal microscopy. (*B*) Inset from *A* showing a site of local separation (highlighted by white arrow) of CGS and NE at t = 10 s, which disappears by (*C*) time t = 22 s. (*D*) Concurrent contours of CGS (H2B-mCherry) and NE (LMNA-GFP) obtained from *A*. (*Inset*) The region from *B* and *C* where CGS and NE locally separate (highlighted by blue arrow). (*E*) Fluctuations u^2 for the contours of CGS and NE from *D*. (*F*) Visualization of the separation sites of CGS and NE, by plotting $(u_{ne} - u_{cgs})^2$ as a function of polar angle ϕ and time t; u_{ne} and u_{cgs} are the deviations of the NE and CGS contours from their respective average contours. The black box highlighted by blue arrow demarks the temporal evolution of the separation site from *D*. The black bracket shows one separation event of duration τ. [Scale bar, (*A*) 5 μm; (*B* and *C*) 2 μm.]

polymerization by latrunculin A ($n = 16$), and myosin II activity by blebbistatin ($n = 15$). We found that both u^2 (Fig. 4*B*) and $\langle u_q^2 \rangle$ (Fig. 4*C*) decrease upon nocodazole and blebbistatin treatment, while they increase upon latrunculin A treatment, implicating cytoskeletal activity. Finally, we probed the involvement of the chromatin by measuring the shape fluctuations of CGS and NE upon inhibition of the polymerase II transcriptional activity by α-amanitin ($n = 15$), which led to an increase in u^2 (Fig. 4*B*) and $\langle u_q^2 \rangle$ (Fig. 4*C*), implying chromatin's participation. When compared against known q dependencies for thermally driven systems, dominated by bending rigidity ($\sim q^{-4}$) and lateral tension ($\sim q^{-2}$) (29), $\langle u_q^2 \rangle$ shows new q dependencies, which might be characteristic of nonequilibrium processes in our system.

To determine the dynamic contributions that became eliminated upon different perturbations, we computed the power spectral density (PSD) as a function of wavelength $\lambda = L_c/q$, where L_c is the contour length (Fig. 4*D*). Inspection of PSD revealed that, for $\lambda < 1.5$ μm, PSD remained unchanged after ATP depletion, nocodazole, blebbistatin, and α-amanitin treatment, suggesting that these fluctuations are mostly thermally driven. This supports our finding that cell cycle-dependent decrease of $\langle u_q^2 \rangle$ at high q is due to the NE stiffening, as this part of the spectra is dominated by thermal fluctuations and follows q^{-4} (Fig. S4 and ref. 29). For $\lambda > 1.5$ μm, we found PSD reduced after ATP depletion, nocodazole, and blebbistatin treatment, while it increased after α-amanitin treatment, suggesting that these fluctuations are actively driven, and thus sensitive to perturbations of involved activities. In contrast, PSD increased for all wavelengths λ after latrunculin A treatment. This is consistent with previous observations of dorsal actin cables, which were shown to hold the nucleus in place, while deforming it to its characteristic ellipsoid shape (30, 31). Hence, upon depolymerization of actin, the nucleus becomes more spherical and visibly softer (Fig. 5*A*).

To gain insight into the molecular mechanism behind the shape fluctuations of CGS and NE, we analyzed the dynamic behavior of both fluctuation sites and separation sites upon all biochemical perturbations (Figs. S5–S7). A summary of r_f, k_f, τ_f and r_s, k_s, τ_s measured for all perturbations is provided in Table S1; here we review our main findings. We find that the fluctuations are driven both actively and passively, evidenced by a decrease in both $\langle u_q^2 \rangle$ and the number of fluctuation sites along the contour after ATP depletion. Furthermore, $\langle u_q^2 \rangle$ and the number of fluctuation sites along the contour decrease after blebbistatin and nocodazole treatment, respectively, suggesting that both microtubules and myosin II activity contribute to shape fluctuations. Conversely, we see an increase in both $\langle u_q^2 \rangle$ and the number of fluctuation sites, upon inhibiting transcriptional activity by α-amanitin, implying chromatin's involvement in shape fluctuations. In addition, while the amplitude of the fluctuations changes upon the perturbations as described above, inward and outward fluctuations remain equally likely. Based on these observations, we speculate that, while both cytoskeleton and chromatin are involved in driving the nuclear shape fluctuations,

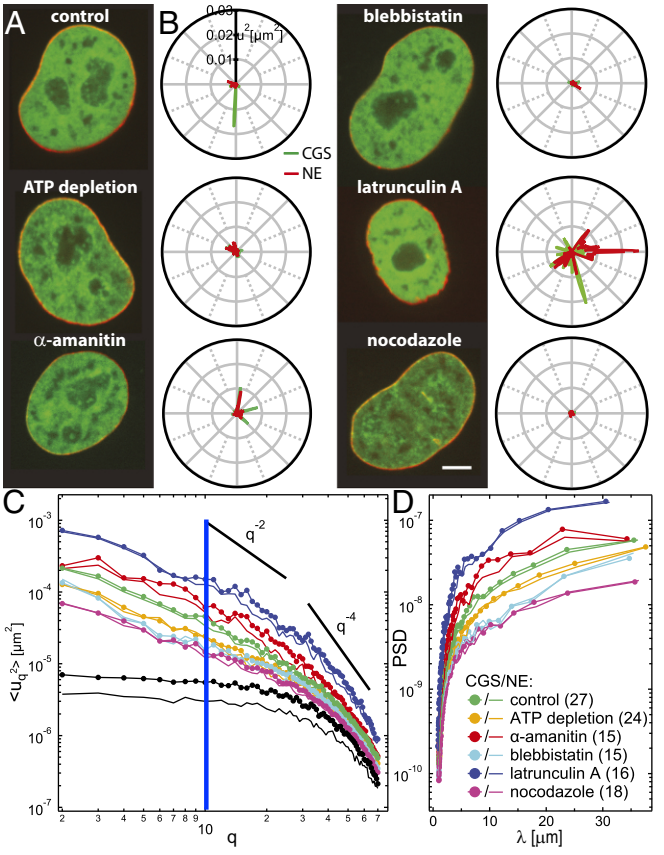

Fig. 4. Simultaneous measurements of shape fluctuations of CGS and NE upon biochemical perturbations. (*A*) Micrographs of cell nuclei expressing both H2B-mCherry (green) and LMNA-GFP (red) under the following conditions: control, after ATP depletion, and upon addition of α-amanitin, blebbistatin, latrunculin A, and nocodazole. (*B*) Fluctuations u^2 of CGS (green) and NE (red) for each condition from *A* at one time point. Average and instantaneous contours for CGS and NE are shown in Fig. S6. (*C*) Wavenumber-dependent $\langle u_q^2 \rangle$ under the following conditions: control (n = 27), ATP depletion (n = 24), α-amanitin (n = 15), blebbistatin (n = 15), latrunculin A (n = 16), and nocodazole (n = 18) treatment. Black curves represent negative control by fixation with formaldehyde for CGS (markers) and NE (no markers). Solid black lines illustrate slopes $\sim q^{-2}$ and $\sim q^{-4}$. Error bars are shown in Fig. S6. (*D*) PSD of $\langle u_q^2 \rangle$ as a function of wavelength λ upon different perturbations. (Scale bar, 5 μm.)

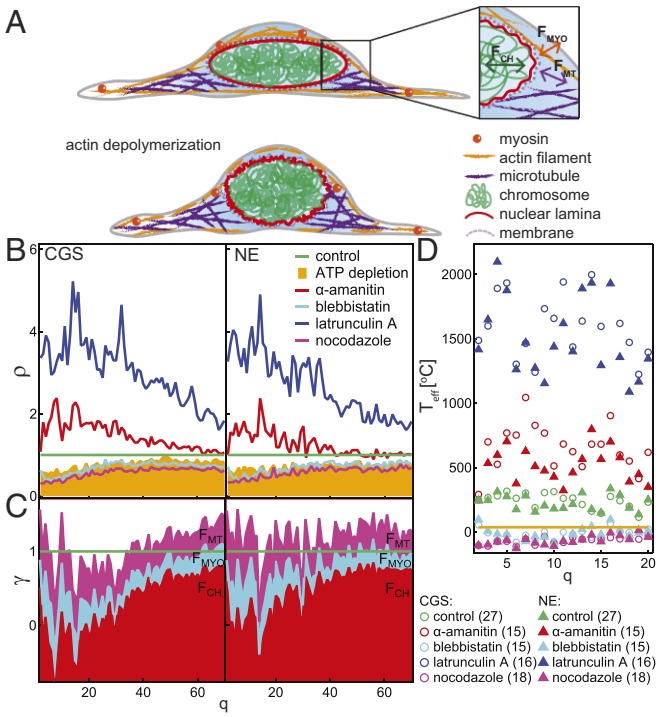

Fig. 5. Active and passive dynamics of CGS and NE. (*A*) Cartoon of a control cell (*Top*) and after actin depolymerization (*Bottom*). *Inset* illustrates the fluctuations of the NE caused by chromatin, F_{ch}, microtubules, F_{mt}, and myosin II, F_{myo}. (*B*) The ratio $\rho = \langle u^2_{q,\,pert}\rangle / \langle u^2_{q,\,control}\rangle$ shows the changes in fluctuations of CGS and NE upon different perturbations. (*C*) Cumulative plot of the passive contribution (baseline $\gamma = \rho_{pass}$) and relative active contributions $\gamma = (\langle u^2_{q,\,control}\rangle - \langle u^2_{q,\,pert}\rangle)/\langle u^2_{q,\,control}\rangle$ of chromatin, microtubules, and myosin II amounts to ∼1. (*D*) T_{eff} for different perturbations.

they might have opposing effects, with cytoskeleton acting as an amplifier and chromatin acting as a damper.

This hypothesis is supported by the evidence that the number of separation sites of CGS and NE increases after ATP depletion, blebbistatin, and nocodazole treatment. In other words, when active fluctuations or cytoskeleton activity are suppressed, NE and CGS tend to move out of phase. In contrast, the number of separation sites decreases upon α-amanitin treatment. This is consistent with previous observations of chromatin decondensation upon α-amanitin treatment (32), effectively increasing the osmotic pressure inside the nucleus, which could lead to more in-phase movement of CGS and NE.

Interestingly, while the number of separation sites changes upon ATP depletion, as well as cytoskeletal and chromatin perturbations, the activity of a separation site remains unchanged under all of these conditions, suggesting that NE is a passive shell sandwiched between two active materials. This is further corroborated by our observation of two different types of activity of the separation sites: short events (<1 s) present under all conditions, including ATP depletion, suggesting these are thermally driven, and long events (>4 s), which are active, i.e., eliminated upon ATP depletion, reduced upon blocking cytoskeletal activity, and enhanced upon blocking the transcriptional activity of chromatin.

Active vs. Passive Fluctuations. Our experiments demonstrate that nuclear shape fluctuations are both thermally and actively driven. The passive thermal fluctuations are visible after ATP depletion, when we find $\langle u^2_q\rangle$ to be reduced by ∼50%. As evidenced by r_f (Table S1), under physiological conditions, about 65% of the contour fluctuates, while it decreases to about 50% upon ATP depletion. These fluctuations are passive, with about one third having NE and CGS fluctuating out of phase ($r_{s,f}$, Table S1).

From our observations, we can estimate the contribution of active vs. passive dynamics. First, the ratio of the fluctuations after a perturbation and the control sample $\rho = \langle u^2_{q,pert}\rangle / \langle u^2_{q,control}\rangle$ provides a measure of the change in the shape fluctuations of CGS and NE with respect to those under physiological conditions (Fig. 5*B*). For latrunculin A, we find a large increase in ρ, which refers to the flickering of the NE after the actin filament depolymerization. In this situation, the nucleus is not under the pressure of dorsal actin cables (30, 31), and thus the observed fluctuations might be informative of its true bending rigidity κ (Fig. 5*A*). After ATP depletion, we find ρ reduced to about 40% at low q and to about 50% at high q, suggesting that up to one half of the observed dynamics is of thermal origin, i.e., passive. Computing ρ for α-amanitin, nocodazole, and blebbistatine, we find an estimate for dynamic contributions of chromatin, microtubules, and myosin II, respectively (Fig. 5*B*). To better visualize these estimates, we calculate their relative contributions $\gamma = (\langle u^2_{q,control}\rangle - \langle u^2_{q,pert}\rangle)/\langle u^2_{q,control}\rangle$ and plot them cumulatively in Fig. 5*C*. The cumulative γ adds up to ∼1, confirming that we identified the major molecular players in the nuclear shape fluctuations. The ratio of their contributions might change during the cell cycle as their activity changes.

Another way to evaluate active fluctuations is to compute the effective temperature T_{eff} that our system would have, if in equilibrium (33). While this assumption is not correct, it allows us to assess how our system deviates from thermal equilibrium. Provided the excitations of active and passive fluctuations are driven independently, then $\langle u^2_q\rangle$ can be expressed as a sum of active and passive fluctuations $\langle u^2_q\rangle = \langle u^2_{q,active}\rangle + \langle u^2_{q,passive}\rangle$ and $T_{eff}/T \simeq \langle u^2_q\rangle / \langle u^2_{q,passive}\rangle = 1 + \langle u^2_{q,active}\rangle / \langle u^2_{q,passive}\rangle$ (33). We find that, under physiological conditions $T_{eff} \approx 300\ ^\circ$C, while it increases to $\sim 500\ ^\circ$C upon inhibiting transcription and falls to $0\ ^\circ$C upon inhibition of microtubule polymerization and myosin II (Fig. 5*D*). Once the actin depolymerizes, both CGS and NE fluctuations are very high, with $T_{eff} \approx 1{,}000\ ^\circ$C to $2{,}000\ ^\circ$C. As a comparison, in red blood cells, T_{eff} was found to be about $3{,}000\ ^\circ$C at low q (33, 34).

Conclusions

Our findings reveal that NE flickers, i.e., undulates at time scales of seconds, with active undulations driven by both chromatin and cytoskeleton. The amplitude of these undulations provides us with an internal cell cycle stage indicator. The possible role of such undulations is yet to be revealed. Considering the complex structure of the NE, specifically its dense coverage with nuclear pores (five to seven pores per square micrometer) (35), we speculate that such undulations might aid nuclear transport. In fact, it has been shown previously that oscillating a membrane enhances flux through its pores (36, 37). Such undulations could facilitate a more effective stirring of the molecules in the NE vicinity, and thus their faster binding to importins/exportins. Also, the NE undulations could influence flows into and out of the cell nucleus and accelerate otherwise diffusion limited processes. Such flows, in turn, would lead to the transport of material that may cause osmotic pressure (and even Donnan potential) fluctuations across the NE. Such fluctuations are not considered in current models of nuclear transport (38–40).

Materials and Methods

Cell Culture and Cell Transfection. HeLa cells (CCL-2) were cultured according to American Type Culture Collection (ATCC) recommendations. The stable HeLa LMNA-GFP and HeLa H2B-GFP cell lines were a gift from Tim Mitchison and James Orth, Harvard Medical School, Boston. Cells were cultured in a humidified, 5% CO_2 (vol/vol) atmosphere at 37 °C in Gibco Dulbecco's modified eagle medium supplemented with 10% FBS (vol/vol), 100 units per milliliter of penicillin, 100 mg/mL of streptomycin (Invitrogen), and 2.5 mg/mL of Plasmocin Prophylactic (Invivogen). Before the experiment, cells were plated on 35-mm MatTek dishes with glass bottom no.

1.5 (MatTek) for 24 h, and the medium was then replaced by Gibco CO_2-independent medium supplemented with L-glutamine (Invitrogen). Cells were then mounted on the microscope stage kept in a custom-built 37 °C microscope incubator enclosure with 5% CO_2 (vol/vol) delivery during the entire experiment. When specified, cells were synchronized using 10 μM RO-3306 (ALEXIS), which arrests cells at the G2/M checkpoint of the cell cycle, and were released, 1 h before imaging, by washing with CO_2-independent medium supplemented with L-glutamine. For fixation experiments, cells were fixed with 3.7% formaldehyde in PBS at room temperature for 20 min and then washed three times with PBS every 5 min. Coverslips were mounted on the glass microscope slides, using Prolong-Diamond antifade reagent (Invitrogen). HeLa cells expressing LMNA-GFP and H2B-mCherry were prepared by transient transfection of the stable HeLa LMNA-GFP cell line with H2B-mCherry plasmid using Lipofectamine 2000 (Invitrogen) following the manufacturer's protocol.

Biochemical Perturbations. To deplete ATP, cells were treated, 2 h before imaging, with 6 mM 2-deoxyglucose and 1 μM trifluoromethoxy-carbonylcyanide phenylhydrazone dissolved in CO_2-independent medium supplemented with L-glutamine. For cytoskeletal perturbations, 10 μM latrunculin A, 10 μM blebbistatin, or 10 μM nocodazole, and, for chromatin perturbations, 20 μg/mL α-amanitin, in CO_2-independent medium supplemented with L-glutamine, were added to cells 30 min before imaging. All chemicals are from Sigma-Aldrich.

Microscopy and Image Acquisition. Images were taken with a Yokogawa CSU-X1 spinning-disk confocal head with an internal motorized high-speed emission filter wheel and Spectral Applied Research Borealis modification for increased light throughput and illumination homogeneity on a Nikon Ti-E inverted microscope equipped with a 100× Plan Apo NA 1.4 objective lens and the Perfect Focus System. The microscope was mounted on a vibration-isolation air table. LMNA-GFP and H2B-GFP fluorescence were excited by a 488-nm solid-state laser (controlled with an acousto-optic tunable filter) and collected with a 405/488/561/640 multiband-pass dichroic mirror (Semrock) and an ET525/50 emission filter (Chroma Technology). To image GFP and mCherry at the same time, we illuminated the sample simultaneously with two excitation wavelengths, 488 and 561 nm, produced by two distinct monochromatic solid-state lasers. The emission was separated by the W-View Gemini Image Splitter (Hamamatsu) using GFP/mCherry dichroic mirror (Chroma Technology), and further passed through an ET525/30 and an ET630/75m emission filter (Chroma Technology). The two fluorescent signals were allocated to the two halves of the image sensor, producing two distinct images. Images were obtained with a Hamamatsu ORCA-R2 cooled CCD camera controlled with MetaMorph 7 (Molecular Devices) software. The pixel size for the 100× objective was 0.065 μm. The observation duration was 25 s, with an exposure time of 250 ms. The streams of 16-bit images were saved as multi-tiff stacks. Images were converted to single-tiff images and analyzed in MatLab (The MathWorks). To detect a nuclear contour and analyze its shape fluctuations, we used a custom-written MatLab code (see *SI Materials and Methods* and Fig. S8).

ACKNOWLEDGMENTS. This research was supported by the National Institutes of Health (Grant R00-GM104152).

1. Steen H, Lindmo T (1978) Cellular and nuclear volume during the cell cycle of nihk 3025 cells. *Cell Tissue Kinet* 11:69–81.
2. Fidorra J, Mielke T, Booz J, Feinendegen L (1981) Cellular and nuclear volume of human cells during the cell cycle. *Radiat Environ Biophys* 19:205–214.
3. Alberts B, et al. (2014) *Molecular Biology of the Cell* (Garland Sci, New York).
4. Talwar S, Kumar A, Rao M, Menon G, Shivashankar G (2013) Correlated spatiotemporal fluctuations in chromatin compaction states characterize stem cells. *Biophys J* 104:553–564.
5. Makhija E, Jokhun D, Shivashankar G (2015) Nuclear deformability and telomere dynamics are regulated by cell geometric constraints. *Proc Natl Acad Sci USA* 13: E32–E40.
6. Brochard F, Lennon J (1975) Frequency spectrum of the flicker phenomenon in erythrocytes. *J Phys* 36:1035–1047.
7. Duwe H, Sackmann E (1990) Bending elasticity and thermal excitations of lipid bilayer vesicles: Modulation by solutes. *Phys Stat Mech Appl* 163:410–428.
8. Zidovska A, Sackmann E (2006) Brownian motion of nucleated cell envelopes impedes adhesion. *Phys Rev L* 96:048103.
9. Watson M (1954) The nuclear envelope: Its structure and relation to cytoplasmic membranes. *J Biophys Biochem Cytol* 1:257–270.
10. Cohen A, Sundeen J (1976) The nuclear fiburous lamina in human cells: Studies on its appearance and distribution. *Anat Red* 186:471–476.
11. Dahl K, Kahn S, Wilson K, Disher D (2004) The nuclear envelope lamina network has elasticity and a compressibility limit suggestive of a molecular shock absorber. *J Cell Sci* 117:4779–4786.
12. Lammerding J, et al. (2006) Lamins A and C but not lamin B1 regulate nuclear mechanics. *J Biol Chem* 281:25768–25780.
13. Rowat A, Lammerding J, Ipsen J (2006) Mechanical properties of the cell nucleus and the effect of emerin deficiency. *Biophys J* 91:4649–4664.
14. Davis L, Blobel G (1986) Identification and characterization of a nuclear pore complex protein. *Cell* 45:699–709.
15. Wente S, Rout M (2010) The nuclear pore complex and nuclear transport. *Cold Spring Harb Perspect Biol* 2:a000562.
16. Aaronson R, Blobel G (1974) Isolation of nuclear pore complexes in association with a lamina. *Proc Natl Acad Sci USA* 72:1007–1011.
17. Fowler P, et al. (2016) Membrane stiffness is modified by integral membrane proteins. *Soft Matter* 12:7792–7803.
18. McGarry TJ, Kirschner MW (1998) Geminin, an inhibitor of DNA replication, is degraded during mitosis. *Cell* 93:1043–1053.
19. Wilson K, Foisner R (2010) Lamin-binding proteins. *Cold Spring Harb Perspect Biol* 2:a000554.
20. Méjat A, Misteli T (2010) LINC complexes in health and disease. *Nucleus* 1:40–52.
21. Schreiner S, Koo P, Zhao Y, Mochrie S, King M (2014) The tethering of chromatin to the nuclear envelope supports nuclear mechanics. *Nat Commun* 6:7159.
22. Kind J, et al. (2013) Single-cell dynamics of genome-nuclear lamina interactions. *Cell* 153:178–192.
23. Kumaran R, Spector D (2008) A genetic locus targeted to the nuclear periphery in living cells maintains its transcriptional competence. *J Cell Biol* 180:51–65.
24. Finlan L, et al. (2008) Recruitment to the nuclear periphery can alter expression of genes in human cells. *PLoS Genet* 4:e1000039.
25. Reddy K, Zullo J, Bertolino E, Singh H (2008) Transcriptional repression mediated by repositioning of genes to the nuclear lamina. *Nature* 452:243–247.
26. Worman H, Ostlund C, Wang Y (2010) Diseases of the nuclear envelope. *Cold Spring Harb Perspect Biol* 2:a000760.
27. Broers J, et al. (2004) Decreased mechanical stiffness in LMNA-/- cells is caused by defective nucleo-cytoskeletal integrity: Implications for the development of laminopathies. *Hum Mol Genet* 13:2567–2580.
28. Moir R, Yoon M, Khuon S, Foldman R (2000) Nuclear lamins A and B1: Different pathways of assembly during nuclear envelope formation in living cells. *J Cell Biol* 151:1155–1168.
29. Helfrich W (1978) Steric interaction of fluid membranes in multilayer systems. *Z Naturforsch A* 33:305–315.
30. Khatau S, et al. (2009) A perinuclear actin cap regulates nuclear shape. *Proc Natl Acad Sci USA* 106:19017–19022.
31. Burnette D, et al. (2014) A contractile and counterbalancing adhesion system controls the 3D shape of crawling cells. *J Cell Biol* 205:83–96.
32. Zidovska A, Weitz D, Mitchison T (2013) Micron-scale coherence in interphase chromatin dynamics. *Proc Natl Acad Sci USA* 110:15555–15560.
33. Gov N (2004) Membrane undulations driven by force fluctuations of active proteins. *Phys Rev L* 93:268104.
34. Rodríhuez-García R, et al. (2015) Direct cytoskeleton forces cause membrane softening in red blood cell. *Biophys J* 108:2794–2806.
35. Maeshima K, et al. (2010) Nuclear pore formation but not nuclear growth is governed by cyclin-dependent kinases (Cdks) during interphase. *Nat Struct Mol Biol* 17: 1065–1072.
36. Gomaa H, Rao S (2011) Analysis of flux enhancement at oscillating flat surface membranes. *J Membr Sci* 374:59–66.
37. Menais T, Mossa S, Buhot A (2016) Polymer translocation through nano-pores in vibrating thin membranes. *Sci Rep* 6:38558.
38. Milles S, et al. (2015) Plasticity of an ultrafast interaction between nucleoporins and nuclear transport receptors. *Cell* 163:734–745.
39. Beck M, Hurt E (2016) The nuclear pore complex: Understanding its function through structural insight. *Nat Rev Mol Cell Biol* 18:73–89.
40. Raveh B, et al. (2016) Slide-and-exchange mechanism for rapid and selective transport through the nuclear pore complex. *Proc Natl Acad Sci USA* 113:E2489–E2497.
41. Loftus AF, Noreng S, Hsieh VL, Parthasarathy R (2013) Robust measurement of membrane bending moduli using light sheet fluorescence imaging of vesicle fluctuations. *Langmuir* 29:14588–14594.
42. Lipowsky R (1995) Generic interaction of flexible membranes, *Structure and Dynamics of Membranes*, Handbook of Biological Physics (Elsevier, AmsterdamVol 6, pp 521–602.